

Performance of the second Deep Inelastic Neutron Scattering spectrometer at the Bariloche electron LINAC

This article has been downloaded from IOPscience. Please scroll down to see the full text article.

2013 JINST 8 P08016

(<http://iopscience.iop.org/1748-0221/8/08/P08016>)

View [the table of contents for this issue](#), or go to the [journal homepage](#) for more

Download details:

IP Address: 200.0.233.52

The article was downloaded on 28/08/2013 at 15:45

Please note that [terms and conditions apply](#).

Performance of the second Deep Inelastic Neutron Scattering spectrometer at the Bariloche electron LINAC

L.A. Rodríguez Palomino,^a J.J. Blostein^a and J. Dawidowski^{a,b,1}

^a*Consejo Nacional de Investigaciones Científicas y Técnicas,
Centro Atómico Bariloche and Instituto Balseiro, Universidad Nacional de Cuyo,
(8400) Bariloche, Argentina*

^b*Comisión Nacional de Energía Atómica,
(8400) Bariloche, Argentina*

E-mail: javier@cab.cnea.gov.ar

ABSTRACT: We report on the new Deep Inelastic Neutron Scattering detector bank recently implemented at the Bariloche electron LINAC. We show the characterization and calibration process carried out, which comprises the determination of the detector bank efficiency, and the evaluation of the performance of the filter difference technique. As part of the benchmarking process, polyethylene spectra were measured and analyzed, and the scattering cross sections for carbon and hydrogen were determined in the process. With the addition of this new detector bank to the existing one, we evaluate the combined capacity of the two banks.

KEYWORDS: Data processing methods; Instrumentation for neutron sources; Neutron detectors (cold, thermal, fast neutrons); Gaseous detectors

¹Corresponding author.

Contents

1	Introduction	1
2	Fundamentals	2
3	Experimental setup	3
3.1	Detector bank	3
3.2	Neutron beam	4
3.3	Data collection	4
4	Spectrometer characterization	5
4.1	Incident spectrum	5
4.2	Determination of the spectrometer efficiency	6
5	Performace of the filter difference technique	8
6	Data analysis	9
7	Discussion and conclusions	11

1 Introduction

A new detector bank for Deep Inelastic Neutron Scattering (DINS) experiments was built at the Bariloche electron LINAC facility, where there is already in use another bank formed by 10 cylindrical ^3He detectors at 10 bar pressure, forming a regular decagon around the beam center, as previously described [1]. The new detector bank consists of an array of 12 ^3He detectors at 20 bar pressure forming a regular dodecagon. The sample is placed along the axis of symmetry, and thus neutrons scattered at a constant angle are observed.

The choice of the detector type for this new bank is based on several considerations. Previous experiments showed that the ^3He proportional counters are the most convenient for DINS, since (because of its low atomic number) they are highly insensitive to gamma radiation generated during the LINAC operation. Although ^6Li scintillators are more efficient in the epithermal range, they are very sensitive to gamma radiation generated by the LINAC, which requires placing lead shielding around the detector, thus degrading the angular resolution. Furthermore, scintillation detectors (either ^6Li , or the combination of resonant filters and scintillators as in spectrometer VESUVIO [2]), show a background effect that depends on the filter and sample position [3]. Thus the choice of ^3He detectors at 20 bar pressure was a fair alternative on the premise of increasing efficiency in the epithermal range, while maintaining a reasonable cost.

In previous analysis when we presented the DINS bank of 10 detectors, we represented the diversity of existing scattering angles in our experimental setup by an average effective angle [4].

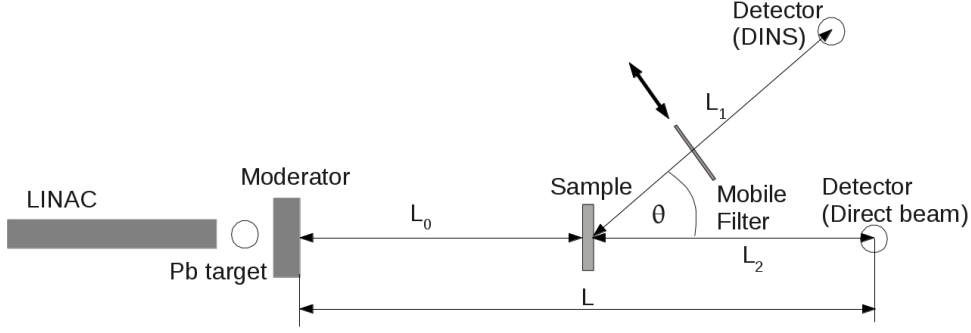


Figure 1. Schematic diagram showing our DINS experimental setup. The distances and scattering angle referred to in the text are displayed. Also shown is the detector placed in direct beam position, employed to determine the incident spectrum.

This approach works well enough for H at room temperature because DINS spectra are broad in time and are dominated by the dynamics of the sample, and not by the uncertainty of the bank angle or the energy width of the filter. However, if we wish to analyze the case of H at low temperatures and also for heavier nuclei at room temperature, the uncertainty of the instrument is evidenced in the spectra. For this reason, the new detector ring was designed to improve the angular uncertainty compared to the pre-existing bank [1].

In this work we show the main features and the performance and calibration process followed to characterize the new detector bank. As in ref. [1], we put special emphasis in a detailed determination of the instrumental characteristics in order to carry out the absolute normalization process.

2 Fundamentals

The basics of DINS were described elsewhere [5], so we shall only give a brief overview. Figure 1 shows the basic setup of a DINS experiment. Neutrons emitted by a pulsed source travel a distance L_0 to the sample, and from there a distance L_1 to the detector, placed at an angle θ with respect to the direction of incident neutrons. A mobile filter is placed in the path of the scattered neutrons and alternative 'filter-out' and 'filter-in' spectra measurements are performed. The difference between these spectra as a function of the neutron time of flight is the basic magnitude determined in DINS experiments. Its expression is [6]

$$\tilde{c}(t, \theta) \Delta t = \int_{E_{\text{inf}}}^{\infty} dE_0 \Phi(E_0) \frac{d^2 \sigma(E_0, E, \theta)}{d\Omega dE} \varepsilon(E) \left[1 - e^{-nT\sigma_F(E)} \right] \left| \frac{\partial E}{\partial t} \right| \Delta\Omega \Delta t, \quad (2.1)$$

where $\Phi(E_0)$ is the energy dependent incident neutron flux, $\frac{d^2 \sigma(E_0, E, \theta)}{d\Omega dE}$ the double-differential cross section of the sample, $\varepsilon(E)$ the detector efficiency, $(1 - e^{-nT\sigma_F(E)})$ the absorption probability of the resonant filter, characterized by a number density n , a thickness T , and a total cross section $\sigma_F(E)$, and $\Delta\Omega$ the solid angle subtended by the detectors. The lower limit of integration E_{inf} is determined by kinematic conditions.

Eq. (2.1) is strictly valid for single scattering. For a sample of finite dimensions (as is the case of a real experiment), the total count rate recorded by the detectors is composed by singly

and multiply scattered neutrons. These contributions, as well as the detector efficiency corrections must be evaluated by Monte Carlo simulations [1]. After this process, the contribution of the singly scattered neutrons can be determined, and from it the distribution of neutrons emerging from the sample after the first scattering. This magnitude is directly related with the microscopic cross sections to be investigated, through

$$c_1(t, \theta)\Delta t = K \int_{E_{\text{inf}}}^{\infty} dE_0 \Phi(E_0) \frac{\Sigma_{\text{scatt}}(E_0)}{\Sigma_{\text{tot}}(E_0)} (1-t(E_0)) \frac{1}{\sigma_{\text{scatt}}(E_0)} \frac{d^2\sigma}{d\Omega dE} \left[1 - e^{-nT\sigma_F(E)} \right] \left| \frac{\partial E}{\partial t} \right| \Delta\Omega \Delta t \quad (2.2)$$

where K is a scale factor linking the neutron count rate with the theoretical integral, $\Sigma_{\text{scatt}}(E_0)$ and $\Sigma_{\text{tot}}(E_0)$ are respectively the scattering and total macroscopic cross sections, and $t(E_0)$ the sample transmission factor.

Throughout this work we will describe the double-differential cross section $\frac{d^2\sigma(E_0, E, \theta)}{d\Omega dE}$ using a gas model at an effective temperature as described in ref. [7]. This approach proved to be an adequate description at the level of the Monte Carlo code, as was shown in previous works.

3 Experimental setup

3.1 Detector bank

The bank is shown in figure 2, together with the preexisting one described in ref. [1]. It consists of 12 cylindrical detectors arranged in a dodecagonal geometry. The detectors are ^3He proportional counters (LND brand, model LND2525, 1 inch outer diameter, and 8 inches active length each) filled at a pressure of 20 bar, connected in parallel. A dodecagonal aluminum structure, used to hold the detectors and also as electrical ground, contains a common HV cable inside to distribute the high voltage.

The scattering angle can be chosen (according to the experiment requirements) by changing the sample and the detector bank position along the axis of symmetry. In this work we chose 59° in forward scattering direction with respect to the incident beam (thus leaving a mean distance of 74.6 cm from the sample position), to optimize the intensity of scattered neutrons in hydrogen while improving the peak separation with respect to the carbon peak as will be discussed in section 7. The filter we employed in this work was a gold foil 0.0535 mm thick mounted on an aluminum cylinder 130 mm diameter and 50 mm length placed coaxially with the incident beam and mounted over a remote-controlled movable structure, devised to perform filter-in and filter-out alternative measurements. This diameter was designed so as to mainly absorb neutrons scattered towards the detector bank, thus minimizing the filter-dependent background which otherwise could have a significant contribution to the spectra.

Background due to upstream neutrons arriving to the experimental hall was shielded with blocks made of boric acid dissolved in paraffin. Also the epithermal background coming from the downstream direction was shielded with 4 mm thick semi-cylindrical covers made of boraffin [8]. The detectors were also covered with 1 mm thick cadmium cylinders to minimize the background due to thermal neutrons.

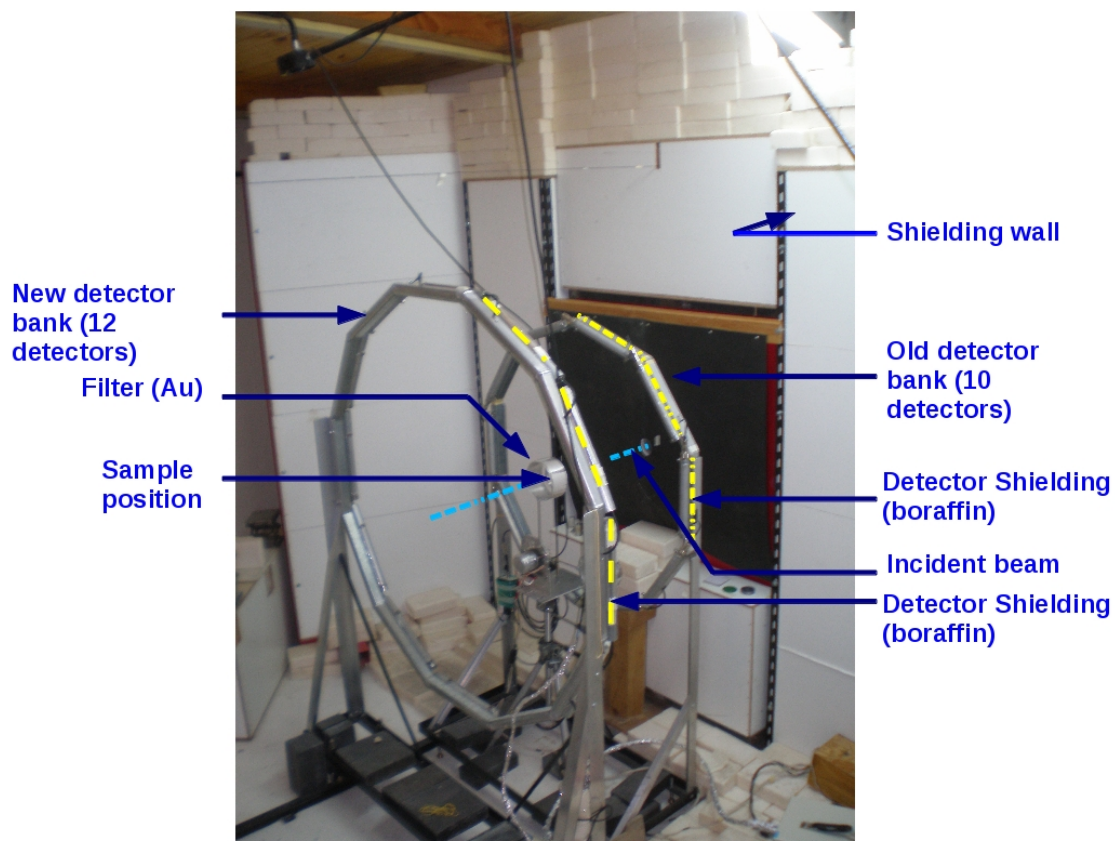


Figure 2. The two detector banks (eVS spectrometer) implemented at Centro Atómico Bariloche, Argentina. The detection angle between incident and the scattered neutrons for the 12-detector bank is 59° .

3.2 Neutron beam

The experiments were performed at the Bariloche linear accelerator (LINAC). Electron pulses of 25 MeV energy and 1 μsec width, were produced at 100 Hz rate with a mean current of 24 μA . The accelerated electrons are stopped in a lead target (4.5 cm diameter and 7 cm length) generating bremsstrahlung radiation, that (in its interaction with the lead nuclei) produces fast neutrons by photo-nuclear effect. The neutrons are moderated in a 4 cm thick polyethylene slab (21 cm \times 21 cm lateral dimensions), producing a pulse of thermal and epithermal neutrons. An epithermal flux was achieved by placing a 1 mm thick cadmium sheet over the moderator exit face, to absorb thermal neutrons. The sample was placed at 512.6 cm from the neutron source. The neutron beam was collimated up to 5.08 cm diameter at the sample position.

3.3 Data collection

Time-of-flight spectra were recorded in 4096 channels, 2 μsec wide each. An independent ^3He detector placed near the neutron source was employed as a monitor, which served to normalize the spectra.

4 Spectrometer characterization

We follow the same characterization scheme described in detail in [1]. As a first step we determined the incident neutron spectrum by placing a reference ^3He detector in the neutron beam, which subsequently allowed us to determine the bank efficiency.

4.1 Incident spectrum

The procedure consists in the following determinations:

Flight path between the neutron source and the detector. The flight path was determined from the peak-maxima times-of-flight of the known resonances of In, Cd, Mo, Ag and Au. The flight path was $L = (778.2 \pm 1.3)$ cm, while the system electronic delay was $t_R = (11.5 \pm 0.4)$ μsec .

Dead time of the detector and its associated electronics. The dead time (τ) of the detector and its data-acquisition electronics line was experimentally determined by transmission of a cadmium circular diaphragm that serves to reduce the count rate in the detector, thus causing different count losses by dead time effect but keeping the shape of the spectrum. To make this measurement we used a thermal incident spectrum, obtained by removing the cadmium plate mentioned in section 3.2 from the incident beam. The transmission of the diaphragm should be a constant if the correct dead-time corrections are applied [1]. The nonparalyzable model [9] with variable τ was applied to the observed transmission spectrum, until a constant was determined. The resulting value was $\tau = 4.6 \pm 0.1$ μsec .

Incident spectrum corrected by detector efficiency. The incident spectrum was measured with the previously characterized detector placed in direct beam position. The background measurement was done by displacing the detector out of the incident beam, and checked by observing the count rate in the transmission of several materials showing saturated absorption resonances. After subtracting background and correcting the spectrum by dead time and electronic delay, we determined the spectrum shown in figure 3.

Determination of flight path lengths and electronic delay of the detector bank The flight path lengths L_0 and L_1 (figure 1) and the electronic delay t_{DB} of the DINS bank, were also determined from the time-of-flight spectra of materials with known resonances. For this we employed a lead sample (essentially an elastic scatterer) and the same set of resonant filter foils mentioned above both inserted in the incident beam in order to "tag" known energies in the time spectrum. To relate the flight distances with the time of flight, we took into account the total flight path and the small inelasticity produced by scattering in the lead target. Then, a neutron with initial energy E_0 (and final energy $E_1 = E_0 f(\theta, A)$) will be detected at a total time-of-flight

$$t = \sqrt{m/2E_0} \left(L_0 + \frac{L_1}{\sqrt{f(\theta, A)}} \right) + t_{DB} \quad (4.1)$$

where $f(\theta, A)$ is the factor that takes into account the inelasticity in the scattering process [1], A the mass of the scattering nucleus in terms of the neutron mass, and θ the scattering angle. For a

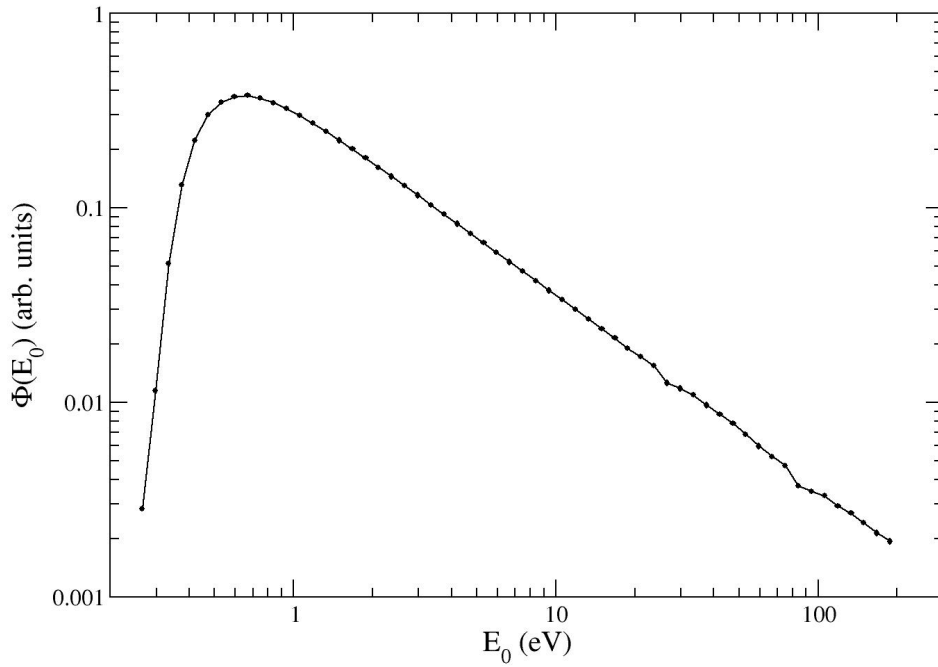


Figure 3. Incident spectrum after correcting by electronic delay, dead time, detector efficiency and background. The drop below 0.6 eV is due to the absorption in the cadmium sheet placed on the moderator face from where the beam was extracted.

lead sample at $\theta = 59^\circ$, the factor $f(\theta, A)$ is 0.9895. The values of the total flight paths and the electronic delay determined by this procedure are

$$\begin{aligned} L_0 &= (512.6 \pm 5.6) \text{ cm} \\ L_1 &= (74.6 \pm 1.0) \text{ cm} \\ t_{DB} &= (16.1 \pm 2.1) \mu\text{sec}. \end{aligned} \quad (4.2)$$

4.2 Determination of the spectrometer efficiency

To determine the spectrometer efficiency, we followed the procedure described in [1]. The process must be performed very carefully because the accurate description of the efficiency is crucial in the data analysis procedure, particularly in the numerical simulations employed to perform the experimental corrections.

The process is based in measuring the spectrum produced by a lead sample. We firstly consider lead as a purely elastic scatterer, so the measured spectrum is directly related with $\Phi(E)$ the incident spectrum previously determined

$$\mathcal{D}_{\text{Pb}}(E) = \varepsilon^0(E)\Phi(E) \quad (4.3)$$

where $\mathcal{D}_{\text{Pb}}(E)$ is the measured Pb spectrum after subtracting the background. From eq. (4.3) we get a zero-order approach of the bank efficiency $\varepsilon^0(E)$.

The second step is to correct the Pb spectrum by multiple scattering and beam attenuation, by means of a recursive method based on Monte Carlo simulations [4, 10]. The zero-order efficiency

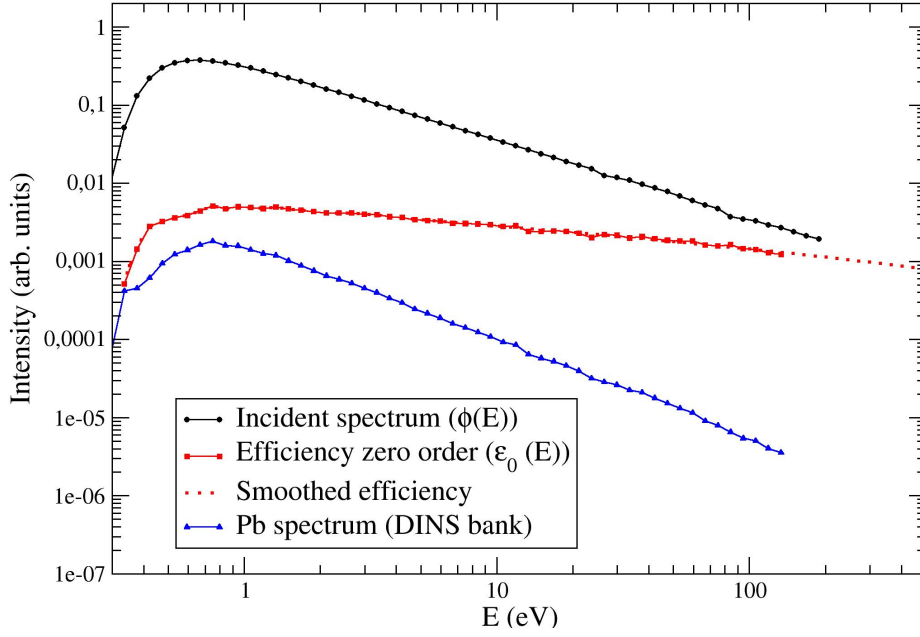


Figure 4. Spectrum $\mathcal{D}_{\text{Pb}}^{(0)}(E)$ from a Pb sample, incident spectrum $\Phi(E)$ and the shape of the efficiency curve $\varepsilon^{(0)}(E)$ (eq. (4.3)), together with its smoothed fitting curve.

$\varepsilon^{(0)}(E)$ is employed in the first Monte Carlo run, from where we determine

$$\mathcal{D}_{\text{Pb}}^{(1)}(t) = F_{\text{corr}}(t) \mathcal{D}_{\text{Pb}}(t). \quad (4.4)$$

where $F_{\text{corr}}(t)$ is the factor employed to correct the Pb spectrum by attenuation and multiple scattering [1].

A new efficiency $\varepsilon^1(E)$ obtained by replacing $\mathcal{D}_{\text{Pb}}(E)$ by $\mathcal{D}_{\text{Pb}}^{(1)}(t)$ in eq. (4.3) is employed in a second run. The recursive process ends when there is no appreciable difference between two consecutive iterations. In the present case convergence was achieved in the second iteration.

It should be noted here that since the method of determining the efficiency we used is based on the measurement of two spectra (eq. (4.3)), and none of them are absolutely determined, neither the efficiency is. That is why in this work we always talk about the shape of the efficiency curve and not of its absolute value. This simple determination is sufficient to implement the calibration method we developed. An absolute determination of the efficiency involves calibrated sources, and is out of the scope of the present work.

For the efficiency measurement, we employed a lead sample 4.8 cm diameter and 1 cm thick, with the filter kept in the “out” position. In figure 4 we show the incident spectrum ($\Phi(E)$), the spectrum resulting from the lead sample ($\mathcal{D}_{\text{Pb}}(t)$) after subtracting background (measured by removing the Pb sample), and the zero-order efficiency ($\varepsilon^{(0)}(E)$) determined according to eq. (4.3). We also show the smoothed efficiency which is used as input in our first Monte Carlo simulations.

The data treatment performed on the Pb spectrum is illustrated in figure 5. Along with the experimental results, we show the total contributions calculated by Monte Carlo, with the efficiencies $\varepsilon^{(0)}(E)$ and $\varepsilon^{(1)}(E)$. We also plot the single and multiple scattering contributions for $\varepsilon^{(1)}(E)$. In the

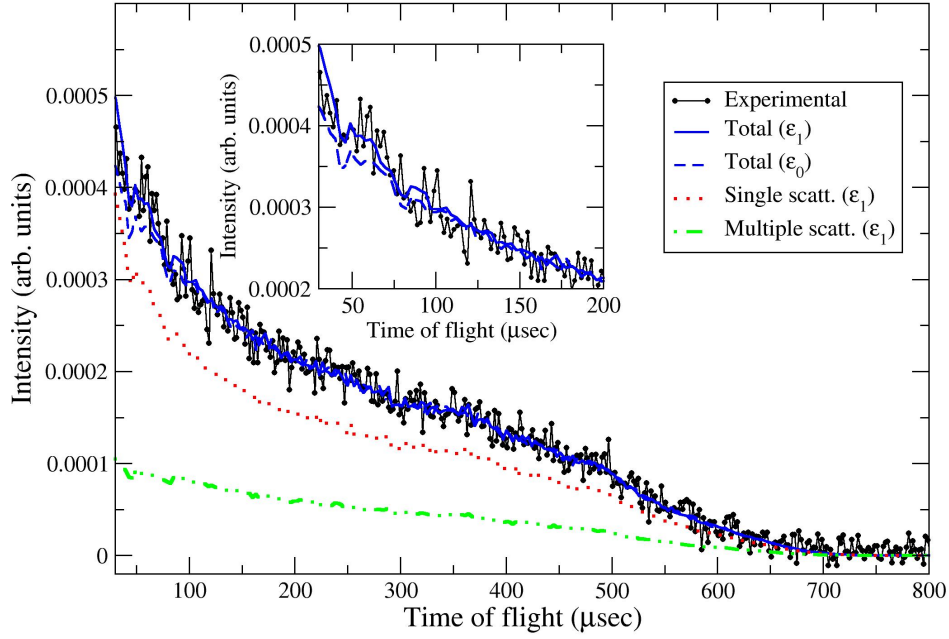


Figure 5. Experimental spectrum from a Pb sample of 4.8 cm diameter and 1 cm thick, compared with Monte Carlo simulations showing the total scattering with efficiency ϵ_0 , and the single, multiple and total scattering contributions with efficiency ϵ_1 . Inset: a zoom of a region of interest where it is possible to observe the differences in the total scattering using ϵ_0 and ϵ_1 .

inset we show a zoom from 30 μsec to 200 μsec , a region in which differences between the spectra calculated with $\epsilon^{(0)}(E)$ and $\epsilon^{(1)}(E)$ are observed. The first 30 μsec of the spectra were not taken into account due to the intense electromagnetic pulse generated by the LINAC, that perturbed the baseline of the acquisition electronics. The efficiencies $\epsilon^{(0)}(E)$ and $\epsilon^{(1)}(E)$ (with their respective smoothed curves) resulting from this process are shown in figure 6.

5 Performace of the filter difference technique

In this section we will show the performance of the filter difference technique [11] of our spectrometer. We will show the absolute calibration carried out, that aims to obtain the cross sections of the constituent elements of the sample. For this purpose we used a coin-shape polyethylene sample, 48 mm diameter and 2 mm thickness, which had been previously characterized by DINS [1] and neutron transmission [12].

Figure 7 displays the experimental neutron Compton profile of Polyethylene, collected after 143 hours of LINAC operation. To reduce possible systematic errors, alternative ‘filter-in’ and ‘filter-out’ measurements were performed every 15 minutes. Time channels were grouped in bins of 4 channels each (8 μsec) and the statistical uncertainty was computed for each one. The graph shows the position of the H and C peaks. Although the last one is not clearly resolved, the comparison with our Monte Carlo calculation confirms the peak position and shows good agreement with the experimental results. We can also observe that the multiple scattering contribution is significant

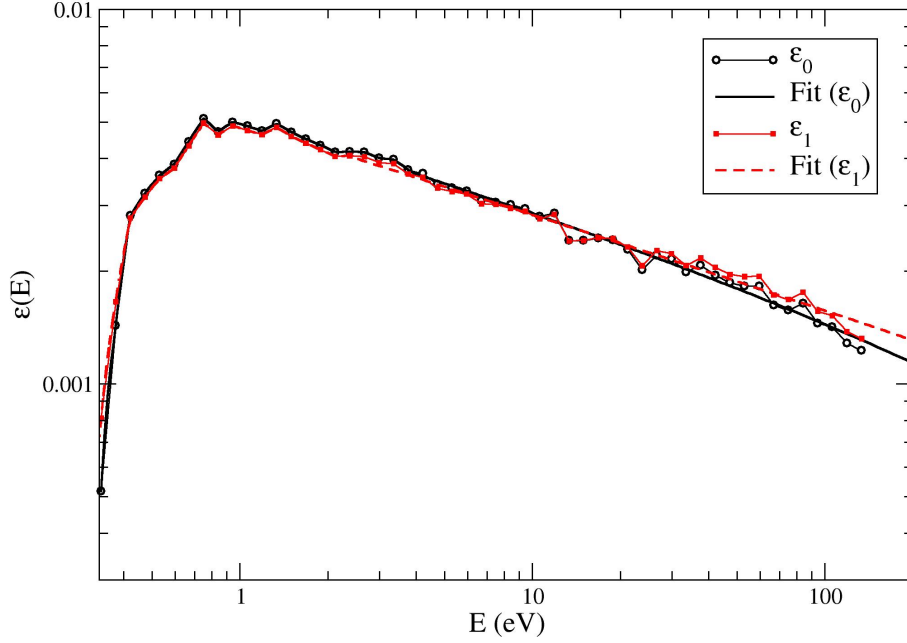


Figure 6. Shapes of the experimental efficiency curves before and after the correction procedure (ϵ_0, ϵ_1) accompanied by their corresponding smoothed curves.

for short times, thus having greater influence in the hydrogen peak (about 10% of the total scattering). The Monte Carlo results were affected by a scale factor 11717 ± 237 (determined by fitting the total calculated scattering with the experimental data by least squares) in order to represent them in the same scale.

The experimental spectrum was corrected by multiple scattering, attenuation and detector efficiency, employing the correction factor method (described in [1]) determined from the Monte Carlo run. After the correction we determined the distribution of neutrons emerging from the sample after the first scattering, described by eq. (2.2), shown in figure 8. A scale factor $K = 20.4 \pm 0.4$ (obtained by least squares) was found to match the theoretical expression (eq. (2.2)) with the experimental results. A good general agreement between simulation and the experimental result is observed.

6 Data analysis

In this section we estimate the relationship between the cross sections of carbon and hydrogen based on our experimental data of polyethylene. The starting point is the expression of the double differential cross section, that as previously mentioned is based on the effective-temperature gas model. Thus, this function can be written as

$$\frac{d^2\sigma(E_0, E, \theta)}{d\Omega dE} = \sqrt{\frac{E}{E_0}} [2\sigma_{b,H} S_H(E_0, E, \theta) + \sigma_{b,C} S_C(E_0, E, \theta)], \quad (6.1)$$

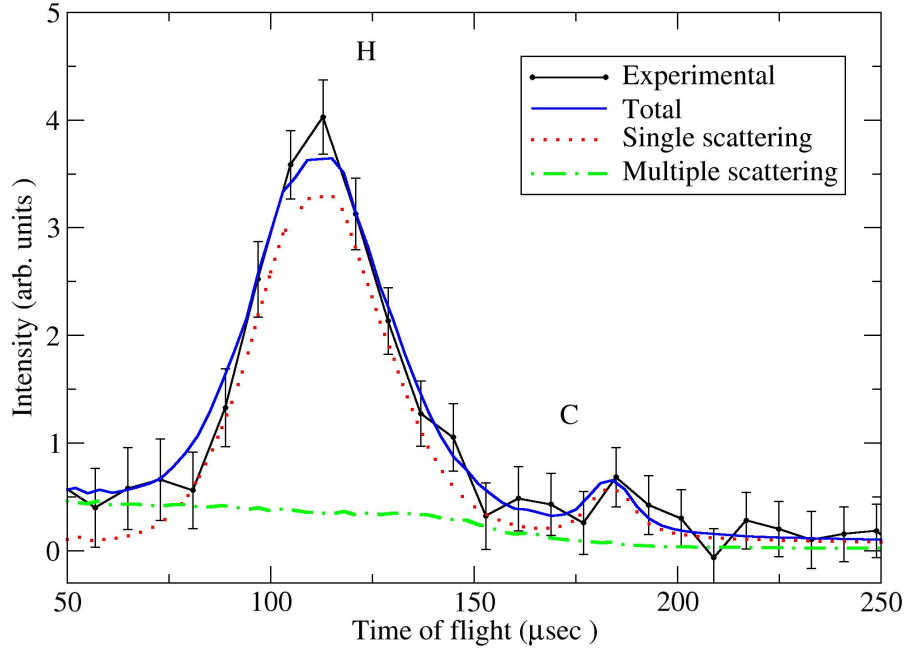


Figure 7. Experimental neutron Compton profile for a polyethylene sample 5 cm diameter and 2 mm thick. The line connecting the points is an eye guide. Monte Carlo simulation show the single, multiple and total scattering contributions. The positions of H and C peaks are indicated.

where $\sigma_{b,X}$ is the tabulated bound-atom cross section and S_X the scattering function for the atom X . Replacing this equation in the eq. (2.2), the neutron Compton profile can be expressed as

$$c_1(t, \theta) = a_H c_H(t, \theta) + a_C c_C(t, \theta), \quad (6.2)$$

where $c_X(t, \theta)$ are the corresponding neutron Compton profile for the atom X and a_X their intensities, that are proportional to their respective bound cross sections expressed in barns. By performing a least-square fit of this expression to the experimental result shown in figure 8, it is possible obtain the intensities a_H and a_C . The values found are: $a_H = 3276 \pm 52$, $a_C = 109 \pm 21$. In figure 9 we show the experimental single scattering spectrum together with the neutron Compton profile corresponding to hydrogen and carbon (eq. (6.2)). There is a general good agreement, but while the statistical uncertainty for a_H is about 1.5%, for the carbon peak a_C it is about 20%. Such large uncertainty, clearly visible in the spectra, could be improved with a longer experiment, which was not considered necessary for the purposes of this work.

Observing eq. (6.1) and by comparing eqs. (6.2) and (2.2), the intensity of hydrogen and carbon peaks are proportional to the number density and the bound-atom cross section, so

$$\begin{aligned} a_H &\propto N_H \sigma_{b,H} \propto 2N \sigma_{b,H} \\ a_C &\propto N_C \sigma_{b,C} \propto N \sigma_{b,C}, \end{aligned} \quad (6.3)$$

where N is the number density of CH_2 units. Thus, the ratio of cross sections ($\sigma_{b,H}/\sigma_{b,C}$) can be

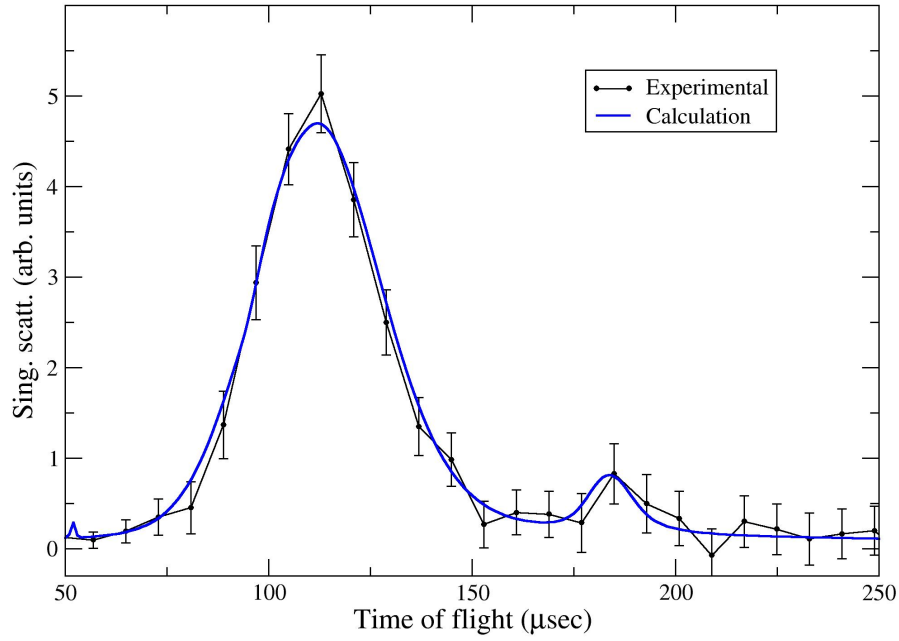


Figure 8. Distribution of neutrons emerging from the sample after the first scattering determined from the experimental data after the correction procedure described in the text. The line connecting the points is an eye guide. This result is compared with our Monte Carlo simulation $c_1(t, \theta)$ (eq. (2.2)), with the factor K determined by a least-squares fitting.

experimentally determined from the ratio of their peak intensities

$$\frac{\sigma_{b,H}}{\sigma_{b,C}} = \frac{a_H}{2a_C} = 15.0 \pm 3.0. \quad (6.4)$$

From standard tables [13] $\sigma_{b,H} = 82.02 \pm 0.06$ barn and $\sigma_{b,C} = 5.551 \pm 0.003$ barn, so $(\sigma_{b,H}/(\sigma_{b,C}))$ is 14.78 ± 0.07 . Although our experimental value is compatible with tables, the relatively large statistical (20%) uncertainty, is mainly due to the significant uncertainty in the carbon peak, as already commented.

7 Discussion and conclusions

In this paper we have shown the performance of our new bank of 12 ^3He detectors, dedicated to the DINS technique, designed to work along with the previously existing one of 10 detectors. To appreciate the current capacity of our detection system, in figure 10 we show the result of Polyethylene above referred together with the measurement performed with the 10-detector bank. Both results correspond to the distribution of singly scattered neutrons, determined after the correction procedure described above. In table 1 we compare the working parameters of both measurements. The path lengths and scattering angle of the 10-detector bank is similar as those reported in ref. [1]. For the latter data we performed a similar analysis as treated in section 6, that yielded $a_H = 1376 \pm 21$ and $a_C = 50 \pm 6$. Thus, the ratio of cross sections $(\sigma_{b,H}/\sigma_{b,C})$ results 13.8 ± 1.7 , in agreement with tabulated values. While the relative error in the determination of the H peak intensity

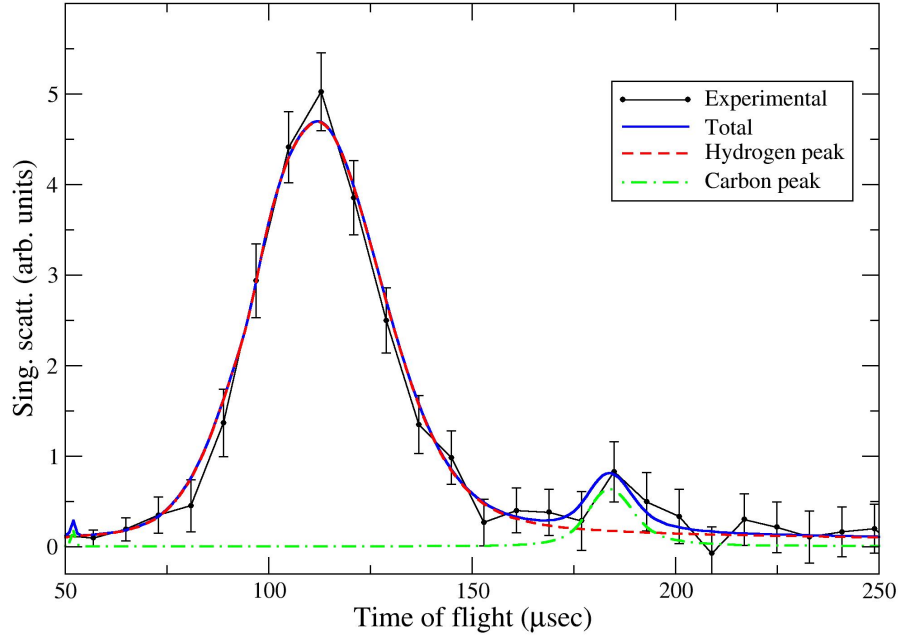


Figure 9. Experimental single scattering spectrum of Polyethylene. The line connecting the points is an eye guide. The Monte Carlo simulation shows the contribution due to hydrogen ($a_{HCH}(t, \theta)$) and carbon ($a_{CCC}(t, \theta)$) peaks, and the total contribution ($c_1(t, \theta)$).

Table 1. Work parameters of the two DINS detection banks operative at the Bariloche electron LINAC, employed in the measurements shown in figure 10.

	10-detector	12-detector
L_0 (cm)	499.0 ± 3.9	512.6 ± 5.6
L_1 (cm)	49.4 ± 0.5	74.6 ± 1.0
Angle (degrees)	70.08 ± 0.69	59.00 ± 0.47

is similar in both measurements (1.5 %), in the C peak they are 12% for the 10-detector bank and 19% for the 12-detector bank. The cause of the larger errors that result in the latter case must be sought in the secondary path length L_1 that due to its geometry is necessarily greater in the 12 detector bank, which causes a loss of intensity that is particularly noticeable in the statistics of the C peak. This loss must be compensated with longer measurements, if the experiment demands it. In compensation this peak is better resolved, due to the larger separation with respect to the H peak that is attained. To illustrate this point, in the inset of figure 10 we show two calculated spectra of Polyethylene for the 10-detector bank placed at 70° (normal working position) and at 59° . We observe that the C peak maximum shifts from 170 to 174 μsec , while the H peak maximum moves from 75 to 105 μsec , while the 12-detector bank at 59° has H and C peak maxima at 112 and 183 μsec respectively, which shows its better performance at lower angles.

At this point, it is appropriate to analyze the angular resolution (i.e. the uncertainty in the

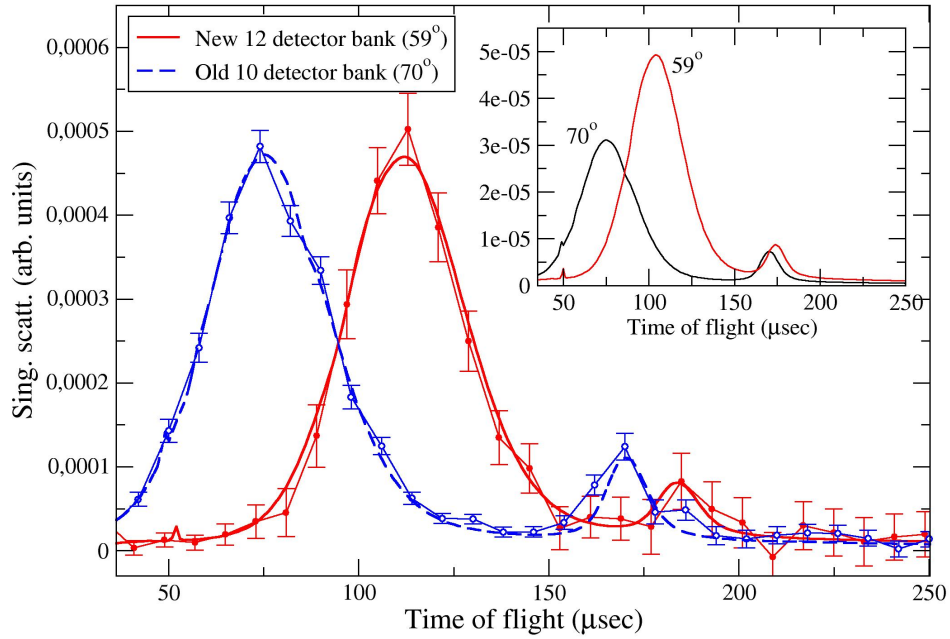


Figure 10. Comparison between Polyethylene neutron Compton profiles, obtained using the new 12-detector bank and the already existing 10 detector bank. The inset shows a calculation of the spectrum of Polyethylene, for the 10-detector bank, placed at two different angles.

scattering angle) of both banks shown in table 1. For this calculation, we examined the detection efficiency as a function of the scattering angle. The calculation was done following ref. [1], taking into account the ^3He absorption cross section as a function of the neutron energy, and the neutron path lengths inside the cylindrical active volume of the detectors. Since the flux of scattered neutrons has a conical symmetry, the path lengths were evaluated from the intersection of cones with vertex in the sample center and variable opening angles. Thus, the efficiency functions (dependent on energy and angle) were defined for both banks, and from them we derived the mean scattering angles and their respective mean square dispersions. Figure 11 represents the result of such calculations for both banks placed in such a way that the center of each detector is at 70° . We can appreciate the lower angular uncertainty of the 12 detector bank, that was one of the design premises mentioned in the introduction, and also the higher efficiency of the 12 detector bank due to its higher gas pressure. We also must emphasize the energy dependence of this function. In the main frame we showed the results for 5 eV neutrons (about the energy of the resonance of the gold filter), and in the inset for 0.01 eV. It is worth noting that this calculation serves only to assess the angular resolution, but that the efficiency used in data processing must necessarily be determined by experiment as explained previously. This is because the actual system is much more complicated, having boraffin and cadmium masks on the detectors, and its interaction with the environment, not taken into account in the elementary calculation.

The addition of the new detector bank presented in this work enables us to expand the capacity of measuring neutron Compton profiles. Since the banks were designed to be mobile, they allow us to work in different configurations. The combination of detection angles shown as examples in

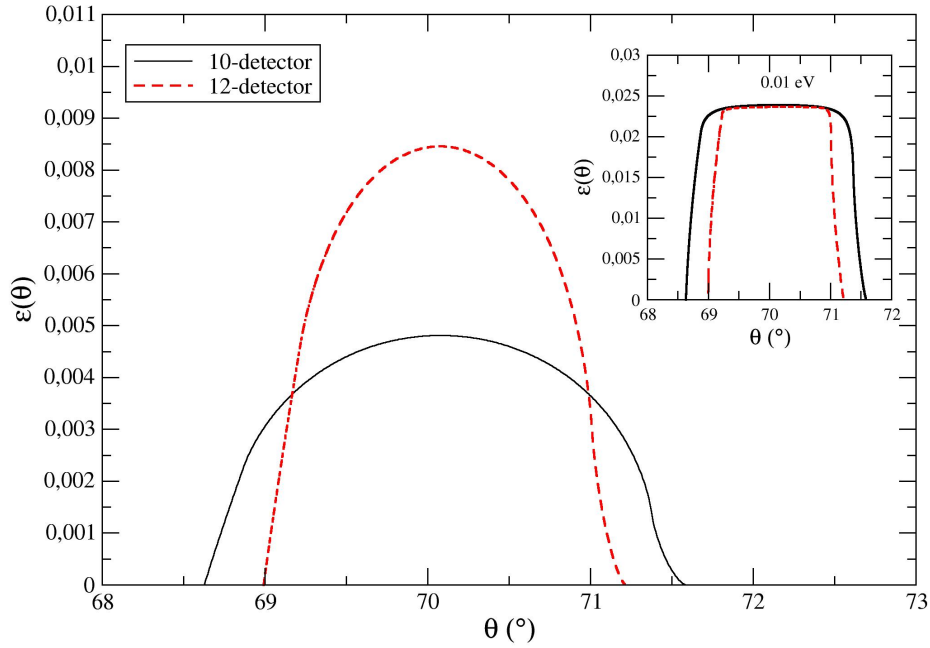


Figure 11. Detection efficiency as a function of scattering angle for the 10 and 12 detector banks. The calculation was made for neutrons of 5 eV. The inset shows the same calculation performed for 0.01 eV neutrons.

this work (both in forward direction) aims at the study of the profiles of hydrogen and light atoms. A combination of forward and backward scattering angles, allow the separate study of the profiles of light and heavy atoms.

Besides its well-known application to the study of momentum distributions, the data analysis system we developed, (described in detail in [1]) allows us to interpret the corrected spectra in terms of the scattering power of the samples in an absolute scale as was shown in ref. [14], where we were able to correlate the hydrogen and deuterium contents in $\text{H}_2\text{O}/\text{D}_2\text{O}$ mixtures. The established method is particularly suitable to determine hydrogen and deuterium contents in metals in a nondestructive way. This is one of the future prospects for use of our detector banks.

Acknowledgments

We gratefully acknowledge L. Capararo and F. Moreira for the technical support, and M. Schneebeli, P. D’Avanzo and A. Mancilla for the LINAC operation.

References

- [1] L.A. Rodríguez Palomino, J.J. Blostein and J. Dawidowski, *Calibration and absolute normalization procedure of a new Deep Inelastic Neutron Scattering spectrometer*, *Nucl. Instrum. Meth. A* **646** (2011) 142.
- [2] J. Mayers et al., *VESUVIO -the double difference inverse geometry spectrometer at ISIS*, *Phys. B Cond. Matt.* **350** (2004) E659.

- [3] J. Mayers, *Calculation of background effects on the VESUVIO eV neutron spectrometer*, RAL Technical Reports, RAL-TR-2010-012 (2010).
- [4] J. Dawidowski, J. Blostein and J. Granada, *Multiple scattering and attenuation corrections in deep inelastic neutron scattering experiments*, [2006 JINST 1 P06002](#).
- [5] C. Andreani, D. Colognesi, J. Mayers, G.F. Reiter and R. Senesi, *Measurement of momentum distribution of light atoms and molecules in condensed matter systems using inelastic neutron scattering*, *Adv. Phys.* **54** (2005) 377.
- [6] J.G. Powles, *The analysis of a time of flight neutron diffractometer for amorphous materials: the structure of a molecule in a liquid*, *Mol. Phys.* **26** (1976) 1352.
- [7] J.J. Blostein, J. Dawidowski and J.R. Granada, *Analysis of mean kinetic energies in H₂O/D₂O mixtures by neutron total cross section measurements*, *Physica* **385B-386B** (2006) 69.
- [8] L.A. Rodríguez Palomino, J.J. Blostein, J. Dawidowski and G.J. Cuello, *Enhanced plastic neutron shielding for thermal and epithermal neutrons*, [2008 JINST 3 P06005](#).
- [9] G.F. Knoll, *Radiation Detection and Measurement*, U.S.A. (1979).
- [10] L.A. Rodríguez Palomino, J. Dawidowski, J.J. Blostein and G.J. Cuello, *Data Processing Method for Neutron Diffraction Experiments*, *Nucl. Instrum. Meth.* **B 258** (2007) 453.
- [11] J. Mayers and A.C. Evans, *Measurement of atomic momentum distribution functions by neutron Compton scattering*, R.A.L. Report RAL-91-048, unpublished (1991).
- [12] J.R. Granada, J. Dawidowski, R.E. Mayer and V.H. Gillette, *Thermal neutron cross section and transport properties of polyethylene*, *Nucl. Instrum. Meth.* **A 261** (1987) 573.
- [13] V.F. Sears, *Neutron scattering lengths and cross sections*, *Neutron News* **3** (1992) 26.
- [14] J. Blostein, L. Rodríguez Palomino and J. Dawidowski, *Measurements of the Neutron Cross Sections of Hydrogen and Deuterium in H O-2 – D O-2 Mixtures Using the Deep Inelastic Neutron-Scattering Technique*, [Phys. Rev. Lett.](#) **102** (2009) 097401.